PCCP

COMMUNICATION

View Article Online
View Journal | View Issue

Check for updates

Cite this: *Phys. Chem. Chem. Phys.*, 2021, **23**, 4480

Received 6th November 2020,
Accepted 5th February 2021

DOI: 10.1039/d0cp05796g

rsc.li/pccp

Spin density localization and accessibility of organic radicals affect liquid-state DNP efficiency†

Marcel Levien, [ab] Maik Reinhard, [ab] Markus Hiller,[a] Igor Tkach, [a] Marina Bennati [ab] and Tomas Orlando *[a]

We report a large variation in liquid DNP performance of up to a factor of about five in coupling factor among organic radicals commonly used as polarizing agents. A comparative study of ^{1}H and ^{13}C DNP in model systems shows the impact of the spin density distribution and accessibility of the radical site by the target molecule.

In the past two decades, dynamic nuclear polarization (DNP) has become one of the most important tools to tackle the long-standing sensitivity issue in modern nuclear magnetic resonance (NMR).[1,2] In a DNP experiment, polarization is transferred from higher polarized electron spins by resonant microwave (mw) irradiation to the target nuclei. Electron spins are often added to the investigated sample in the form of exogenous polarizing agents (PAs), usually organic radicals.

DNP has been successful in the solid-state, where it is routinely applied to various systems in biology and material science, and enables an extraordinary saving of experimental time.[3,4] Part of these achievements were possible thanks to the optimization of bi-radicals as excellent PAs for the polarization transfer *via* cross-effect.[5–7]

The polarization transfer in liquids is dominated by the Overhauser effect (OE)[8] and strongly depends on the chosen target molecule/PA system as well as on the external magnetic field strength.[9,10] Increasing the efficiency of OE-DNP is of particular importance. At high magnetic fields, the choice of an optimal PA would help the application of the method in analytics and high resolution NMR spectroscopy.[11–15] Furthermore, higher NMR enhancements could boost the applications of OE-DNP at low fields (<2 T), which include in-flow hyperpolarization for magnetic resonance imaging[16,17] or chromatography,[18,19] NMR relaxometry of low-γ nuclei,[20] hydration dynamic studies,[21,22] and DNP-NMR spectroscopy.[23–25]

In the experimental practice, nitroxide derivatives (NODs) have been established as optimal PAs for OE-DNP in the liquid state at room temperature and ambient pressure.[26,27] In water, they perform better than trityl radicals at various fields (from 0.34 T to 3.4 T),[28,29] and they are the benchmark for ^{1}H-DNP at low fields (enhancements $\varepsilon = -178 \pm 13$ for water doped with TEMPONE).[30,31] An improvement of nitroxide derivatives performance was realized by linking a C_{60} (fullerene) moiety to a TEMPO based radical, which increased the saturation factor of the electron spin transition.[32] Also **BDPA** has been employed in numerous DNP studies in solid and in liquids, the latter particularly at high fields (≥ 5 T).[14,33,34] However, despite its favourable saturation behaviour, the performance of **BDPA** in liquids as compared to NODs appeared moderate, but a systematic study has been missing.

Despite the available data, it is difficult to compare the PA's performance independently of the experimental conditions, such as mw power and resonant cavity, magnetic field, radical concentration, and target nuclei. Although several mechanistic studies on ^{1}H[27,35,36] and ^{13}C[24,37,38] have been reported, the detailed role of the PA remains unclear. Very recently, we investigated the case of fullerene nitroxides in comparison to TEMPONE,[24,39] and found that small structural reorientations can impact the DNP efficiency at both low and high magnetic fields.[39] Therefore, we proposed that the chemical structure of the PA molecule must play an essential role within the OE-DNP mechanism.

To examine this hypothesis, in this work we systematically investigate and compare the performance of several PAs in OE-DNP in the liquid state and show that NODs, with subtle differences in their chemical structure, behave differently from each other. To ensure comparability of the results, we utilized model solvents in which the polarization transfer mechanisms are known. DNP was performed at low fields (0.34 T and 1.2 T), where an independent determination of all OE parameters was feasible with our available instrumentation. The trend that we

[a] *ESR Spectroscopy Group, Max Planck Institute for Biophysical Chemistry, Am Faßberg 11, Göttigen, Germany. E-mail: tomas.orlando@mpibpc.mpg.de*
[b] *Department of Chemistry, Georg-August-University, Tammannstraße 4, Göttingen, Germany*

† Electronic supplementary information (ESI) available. See DOI: 10.1039/d0cp05796g

Open Access Article. Published on 05 February 2021. Downloaded on 2/8/2026 9:11:54 PM.
This article is licensed under a Creative Commons Attribution 3.0 Unported Licence.

This journal is © the Owner Societies 2021

Open Access Article. Published on 05 February 2021. Downloaded on 2/8/2026 9:11:54 PM.
This article is licensed under a Creative Commons Attribution 3.0 Unported Licence.

observe in DNP performance is interpreted in terms of radical mobility, solvent accessibility, and spin density distributions, with the support of DFT calculations. Our investigation allows to recognize specific characteristics of the PA structure which are a prerequisite for effective OE-DNP in liquids.

Overhauser DNP is based on a cross-relaxation process between an electron spin system and a nuclear spin system mediated by molecular motions.[8,35,40] The hyperfine coupling driving the relaxation consists of two contributions: (i) dipolar coupling, modulated by diffusion;[35,41] (ii) scalar coupling, due to Fermi contact interactions, usually mediated by molecular collisions.[41,42] The complex interplay of these two mechanisms is reflected in a single parameter, the coupling factor ξ, which varies between $\xi = 0.5$ (pure dipolar) and $\xi = -1$ (pure scalar). ξ is defined by the Overhauser equation:[8]

$$\varepsilon = \frac{\langle I_z \rangle}{I_0} = 1 - \xi s f \frac{|\gamma_e|}{\gamma_n}, \quad (1)$$

where ε is the NMR signal enhancement, which is defined as the ratio between the expectation value of the nuclear magnetization under mw irradiation $\langle I_z \rangle$ and the one at thermal equilibrium I_0. γ_e and γ_n are the gyromagnetic ratios of the electron spin (e) and the nuclear spin (n), respectively. The saturation factor s ($0 \leq s \leq 1$) is a measure of how far the electron spin is driven out of equilibrium by the applied mw irradiation.[31] The leakage factor f ($0 \leq f \leq 1$) accounts for the paramagnetic relaxation contribution to the nuclear relaxation term, and depends on the PA concentration. Since s and f can be tuned by the mw power and the radical concentration, respectively, the coupling factor ξ defines the net efficiency of a specific PA in a given system, and can be calculated with eqn (1) once s, f, and ε are independently determined.

In this study, we compare the DNP efficiency, represented by ξ, of six organic radicals that differ in their chemical structure (Fig. 1). Within the NODs, **TL** and **TN** have both a six-membered ring but a different backbone. **DTBN** lacks the piperidine backbone and is therefore very mobile, a feature that, in principle, makes this radical ideal for DNP modulated by fast diffusion processes. In contrast, **TN-py** has the same backbone structure of **TN** but has two hydropyrane rings in the direct vicinity of the NO group.[51] We also consider the fullerene-nitroxide **FN-2a**, which has been already reported as a PA in the context of ^{1}H and ^{13}C DNP.[24,32,39] Finally, we compared NODs with **BDPA**. The organic radicals were dissolved in toluene (C_7H_8), chloroform ($CHCl_3$) and tetrachloromethane (CCl_4), with concentrations in the range 1.5–10 mM. All samples were degassed with freeze-pump-thaw cycles and sealed in quartz tubes.

^{1}H-DNP measurements were performed in toluene and chloroform at 0.34 T. ^{13}C-DNP was performed at 1.2 T in $^{13}CCl_4$ and $^{13}CHCl_3$ samples, and, in order to limit the temperature raise, we worked under low power condition (<3 W). The polarization build-up time was monitored to exclude severe heating effects (ESI†). s and f were measured independently with electron-nuclear double resonance (ELDOR) experiments and nuclear relaxation measurements, respectively (Table 1, and ESI†). NMR enhancements ε were obtained with a mw pumping pulse up to 80 s, depending on the sample. The coupling factor ξ was then calculated with eqn (1).

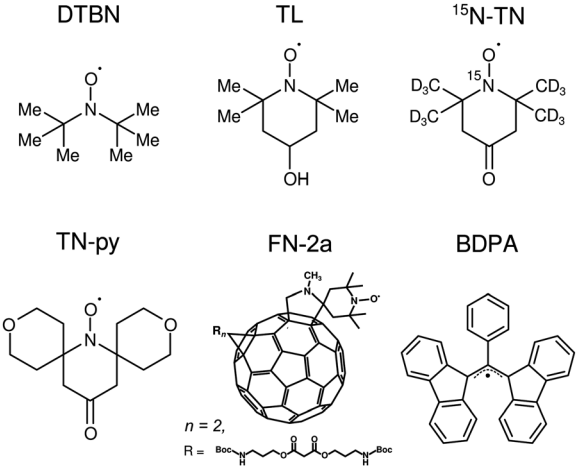

Fig. 1 Molecular structures of the organic radicals tested as PAs for DNP in the liquid state. **DTBN** (di-*tert*-butyl-nitroxide); **TL** (TEMPOL – 4-hydroxy-2,2,6,6-tetramethylpiperidine 1-oxyl); **^{15}N-TN** (^{15}N-TEMPONE-d_{16} – 4-oxo-2,2,6,6-tetramethylpiperidine-d_{16},1-^{15}N-1-oxyl); **TN-py** (7-aza-3,11-dioxa-15-oxodispiro[5.1.5.3]hexadec-7-yl-7-oxyl); **FN-2a**, fullerene-nitroxide derivative with 2 adducts (see inset); **BDPA** (α,γ-bisdiphenylene-phenylallyl).

Table 1 Overhauser parameter f, s, ε and ξ for ^{13}C at 1.2 T and ^{1}H DNP at 0.34 T for different PAs in chloroform. Uncertainties for f and s are 10% while errors for ε and ξ are up to 15% and 25%, respectively (ESI). Radical concentrations are in the range 0.5–16 mM (see ESI for details)

	^{13}C DNP at 1.2 T				^{1}H DNP at 0.34 T			
Radical	$f(^{13}C)$	$s(^{13}C)$	$\varepsilon(^{13}C)$	$\xi(^{13}C)$	$f(^1H)$	$s(^1H)$	$\varepsilon(^1H)$	$\xi(^1H)$
DTBN	0.88	0.04	31	−0.33	0.99	0.76	−181	0.37
^{15}N-TN	0.85	0.18	200	−0.49[24]	0.99	0.92	−224	0.37
TL	0.92	0.07	59	−0.35	0.97	0.45	−85	0.30[39]
TN-py	0.89	0.10	55	−0.23	0.99	0.78	−156	0.31
FN-2a	0.89	0.30	370	−0.53[24]	0.99	0.87	−116	0.20[39]
BDPA	0.40	1.0[a]	122	−0.12	0.99	1.0	−11	0.018

[a] Uncertainty of this measurement is ~15%.

Fig. 2a and b display ξ for ^{13}C and ^{1}H, respectively, in different solvent/PA systems. ^{13}C-DNP coupling factors ξ (Fig. 2a) are negative, a fact which indicates a scalar-dominated polarization transfer,[8,40] and show an interesting, quite unexpected behaviour. Indeed, in CCl_4, ξ is strongly dependent on the PA, and goes from the least efficient **BDPA** ($|\xi| < 0.12$) to the most efficient fullerene nitroxide (**FN-2a**),[24,32] with $|\xi| = 0.65 \pm 0.1$. This indicates a factor of ~5 variation in DNP efficiency. Besides these large differences, also variations among structurally similar small NODs (**TL**, **DTBN** and **TN**) are observed. In $CHCl_3$, the total variation of ξ (from **BDPA** to **FN-2a**) is a factor of ~4 (Table 1), whereas it is a factor of 1.5 among the small NODs ($|\xi|$(**DTBN**) = 0.33 and $|\xi|$(**^{15}N-TN**) = 0.49, Table 1).

^{1}H-DNP coupling factors show a different trend. Firstly, ξ is positive, consistent with a mechanism dominated by dipolar relaxation. Specifically, ξ varies from $\xi = 0.24 \pm 0.04$ for **TN-py** up to a maximum $\xi = 0.42 \pm 0.1$ for **DTBN** in toluene, which is close to the theoretical limit of $\xi = 0.5$.[8,40] Among the NODs, ξ

Open Access Article. Published on 05 February 2021. Downloaded on 2/8/2026 9:11:54 PM.
This article is licensed under a Creative Commons Attribution 3.0 Unported Licence.

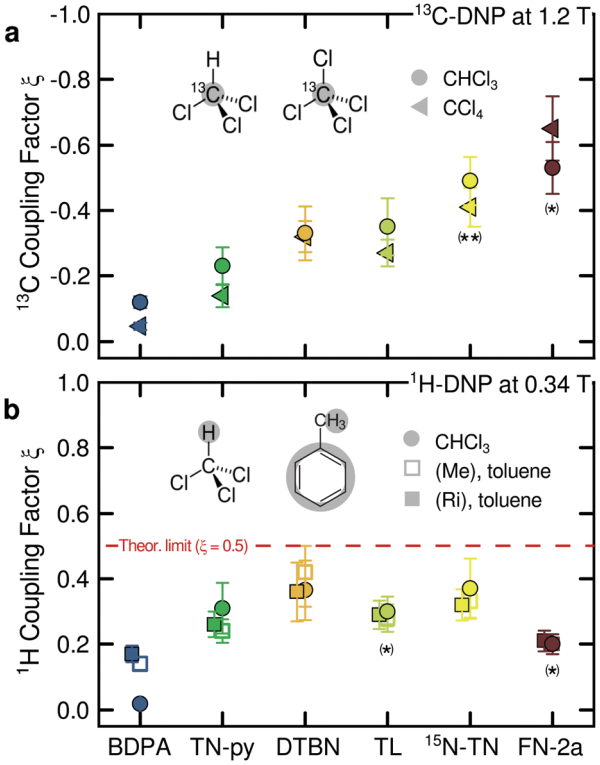

Fig. 2 (a) ^{13}C-DNP coupling factors ξ obtained at 1.2 T for chloroform (circle) and tetrachloromethane (triangle) doped with the organic radicals from Fig. 1. (b) ^{1}H-DNP coupling factors ξ measured at 0.34 T for chloroform and toluene doped with the organic radicals from Fig. 1. Ring (Ri) and methyl (Me) protons of toluene are distinguished. (*) Data from previous reports.[24,32,39] (**) Data reproduced from previous reports.[24]

decreases with larger molecular sizes and the smallest radical, **DTBN**, displays the largest ξ. This behaviour is consistent with the prediction by the force-free hard-sphere (ffHS) model,[43,44] according to which the polarization transfer mediated by dipolar relaxation is modulated by diffusion. Indeed, the efficiency decreases with increasing translational and rotational diffusion time of the PA/target molecule complex. Finally, **BDPA** performs worse than NODs, and shows a solvent dependency for ξ, possibly due to secondary interactions (*e.g.* π-stacking in toluene).

The main question is how to rationalize the trend of the ^{13}C coupling factors shown in Fig. 2a. Indeed, we reported in previous studies,[24,42] and it is predicted by the theory,[8] that the coupling factor in ^{13}C-DNP arises from an interplay of dipolar and scalar relaxations mechanisms.[9,40] First, our results show that poor performance of dipolar dominated DNP (such as ^{1}H-DNP) does not necessarily correlate with an efficient scalar mechanism (Fig. 2). This means that the observed trend reflects a property of the scalar mechanism. Scalar relaxation *via* contact interaction can be described by the Pulse model for random molecular collisions[41] with the spectral density:

$$J_{\mathrm{Pulse}}(\omega_e, A_{\mathrm{FC}}, \tau_{\mathrm{cont}}, \tau_p) = \langle A_{\mathrm{FC}} \rangle^2 \cdot \tau_p^{-1} \cdot \pi^2 \cdot J_{\mathrm{cont}}(\omega_e, \tau_{\mathrm{cont}}), \qquad (2)$$

where ω_e is the Larmor angular frequency of the electron spin, A_{FC} is the isotropic (Fermi Contact, FC) hyperfine coupling (in Hz) modulated by collisions of duration τ_{cont} and collision rate τ_p^{-1}. Accordingly, the scalar mechanism requires that the radical spin density is accessible and transferred to the target nucleus during an encounter.

Hereby, we examined whether the observed trend in ξ could depend on the accessibility of the radical site or on the achievable hyperfine coupling constant or both. For this goal, we analyzed the radical structure as well as the structure of the static PA/target molecule complex using DFT calculations. In the first step, we computed the spin density distribution for each radical optimized structure to identify the radical sites in each PA. In NODs, the electron spin density is almost completely localized on the NO group[38,45] (~90% of the Löwdin spin population, Fig. 3a). In contrast, the majority of the spin population of **BDPA** is localized on the allyl group (~40%), while the remaining spin density is widely distributed over the fluenyl systems (Fig. 3a).[46] It becomes clear that, in the case of **BDPA**, the ffHS model, which defines a single value for the distance of closest approach between the electron spin density and the solvent molecules, is an insufficient approximation.

The spin density distribution was used to identify the radical sites and then calculate their accessibility. We computed the solvent-accessibility surface (SAS) area, a parameter that tracks the center of a spherical probe (the solvent) rolling on the van der Waals surface of the radical. As solvent probes, we considered water (r_{H_2O} = 1.4 Å), for comparison with literature data,[49] and chloroform $CHCl_3$ (r_{CHCl_3} = 3.2 Å). Due to the geometrical nature of SAS areas, the conclusions hold for both solvent probes. Fig. 3b shows that the allyl group in **BDPA** is deeply buried and almost inaccessible, with SAS < 1 Å^2 for both probes. On the contrary, the SAS area of the NO group in the NODs is larger, ranging from a $SAS_{3.2\,Å}$ = 29.5 Å^2 for **DTBN** to $SAS_{3.2\,Å}$ = 35.1 Å^2 for **TN** (Fig. 3b and d). These large SAS areas are mainly due to the accessibility of the O atom, while the N atom remains buried. For **TN-py**, a conformational analysis shows four energetically accessible conformers at room temperature, which differ in the orientation of their hydropyrane rings, *i.e.* open and half-open (ESI†).[49] While $SAS_{3.2\,Å}$ ~ 32 Å^2 for the open conformation, the accessibility of the radical site is hampered in the half-open ones ($SAS_{3.2\,Å}$ ~ 11 Å^2) (Fig. 3c).

Overall, the trend of the SAS depicted in Fig. 3d correlates with our observations of $\xi(^{13}C)$ (Fig. 2a) with the exception of the very large ξ of **FN-2a**. This can be interpreted phenomenologically with the Pulse model for molecular collisions (eqn (2)), which describes $|\xi| \propto J_{\mathrm{Pulse}}$. Intuition suggests that the accessibility of the radical site should mainly impact the collision rate τ_p^{-1}, *i.e.* the likelihood of a given encounter. Since τ_p^{-1} is a prefactor in J_{Pulse}, this could explain the observed correlation. To support this, we note that the field dependent term J_{cont} ($\tau_{\mathrm{cont}}, \omega_e$) in eqn (2) is determined by the duration of each encounter. In previous studies,[24,42] we showed that, in CCl_4 and $CHCl_3$ doped with **TN**, the main contribution comes from $\tau_{\mathrm{cont}} \approx$ 0.5–2 ps. The same could be reasonably assumed for other NODs (**DTBN**, **TL**) in the same solvent and at the same temperature. Nonetheless, structural reorientations on the PA molecule can introduce additional contributions to $J_{\mathrm{cont}}(\tau_{\mathrm{cont}}, \omega_e)$.

This journal is © the Owner Societies 2021

Open Access Article. Published on 05 February 2021. Downloaded on 2/8/2026 9:11:54 PM.
This article is licensed under a Creative Commons Attribution 3.0 Unported Licence.

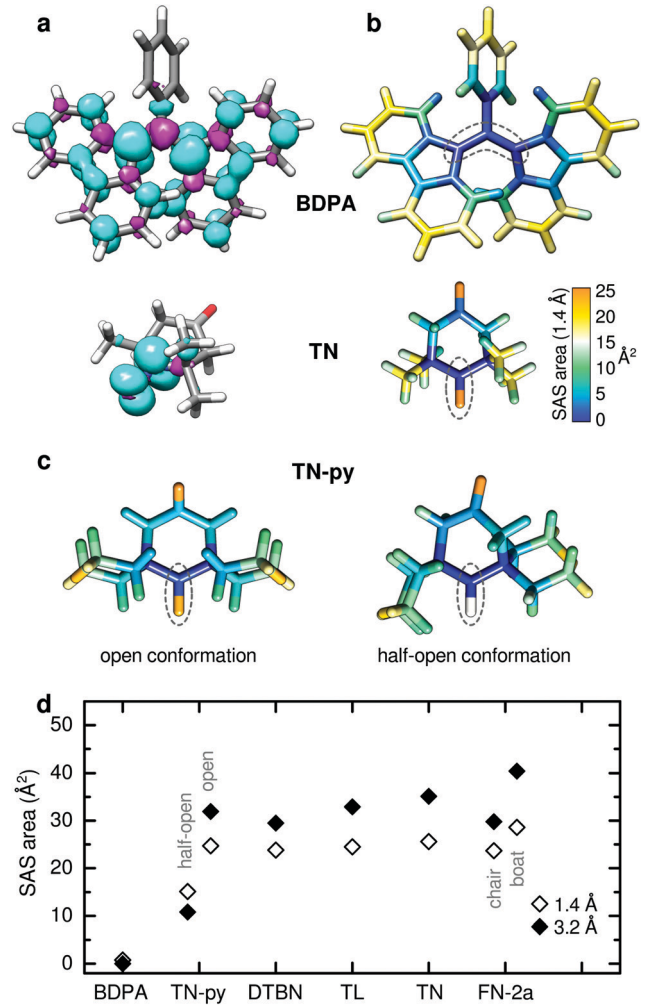

Fig. 3 Geometry optimization and DFT calculations were performed with Orca,[47] using def2-TZVPP as basis set and B3LYP as functional (ESI†). (a) Electron spin density distribution (isosurface threshold $\pm 0.002\,e$ Å^{-3}) calculated for DFT optimized structures of **BDPA** and **TN**. Spin density colour code: cyan: positive, magenta: negative. Atoms colour code: H white, C grey, N blue, O red. (b) Colour map of the SAS area for each atom in **BDPA** and **TN** calculated with a spherical probe of radius 1.4 Å corresponding to the van der Waals sphere of a water molecule. Blue: least accessible; orange: most accessible. Dash lines show the sites with the largest spin density. (c) Colour maps of the SAS areas for **TN-py** in the open conformation (E_{rel} = 0.0 kJ mol^{-1}) and in the half-open conformation (E_{rel} = 0.46 kJ mol^{-1}). The piperidine ring is arranged in a chair for the open conformation and in a twist for the half-open. Graphics and SAS calculations were obtained with UCSF Chimera[48] and Jmol.[52] (d) SAS areas of the radical sites where the largest spin density is localized. Two stable conformations were considered also for **FN-2a**, the most stable one (chair) and the closest in energy (boat), although the latter is not accessible at room temperature.[39]

This is particularly relevant for the specific case of **FN-2a**, whose outstanding performance is likely caused by a particularly favourable collision time scale ($\tau_{cont} \sim$ 4–12 ps) which maximizes $J_{cont}(\omega_e,\tau_{cont})$ at this magnetic field (1.2 T). In our previous report,[39] this was attributed to the transition of the six-membered ring from a chair to an unstable half-chair conformation, enabled by the asymmetry of the backbone linker.[39] Similar dynamics are not expected in **TL**, **TN**, and **DTBN** but cannot be excluded for **TN-py**.

In a second step, we considered the static complex PA/target molecule and used DFT calculations to compute the hyperfine coupling constant A_{FC} to the target nucleus.[38,42] A_{FC} of the C nucleus in $CHCl_3$ was calculated for at least four optimized geometries i for each complex PA/$CHCl_3$ (ESI†). Due to the tendency of the H atom of $CHCl_3$ to form hydrogen bonds, we distinguish an energetically favoured complex where the H is pointing towards the radical ("*via* H"), and a less favoured one, where the Cl atom is the closest to the radical ("*via* Cl"). The hyperfine coupling $\langle A_{FC}\rangle$ was calculated as the weighted average of $A_{FC,i}$ over the relative free energy $E_{rel,i}$ of each configuration i, *i.e.* $\langle A_{FC}\rangle = \sum_i A_{FC,i}\cdot P_i \Big/ \sum_i P_i$ where $P_i = e^{E_{rel,i}/k_B T}$, with T = 300 K. $\langle A_{FC}\rangle$ calculated for **DTBN**, **TL**, and **TN** are similar and between 11.8 MHz and 14.6 MHz. The lack of the piperidine backbone structure in **DTBN** seems to slightly affect the hyperfine coupling to the C nucleus. Notably, the $\langle A_{FC}\rangle$ of **TN-py** calculated for both the open and the half-open conformations are smaller than the other NODs (Fig. 4), which agrees with our experimental observation of a lower $\xi(^{13}C)$. This is justified within the Pulse model, where the spectral density J_{Pulse} scales with $\langle A_{FC}\rangle$ (eqn (2)).

Finally, the $\langle A_{FC}\rangle$ calculated for the complex **BDPA**/$CHCl_3$ is 0.26 MHz, significantly lower than $\langle A_{FC}\rangle$ calculated for NODs (Fig. 4 and ESI†). This reveals the weak ability of **BDPA** to transfer spin density on the C nucleus, despite more than 50% of the spin density is readily accessible on the phenylene rings. Therefore, the lack of an accessible site where a large spin density is localized seems to be detrimental for scalar-driven DNP.

In conclusion, our study revealed that differences in chemical structure of organic PAs commonly used in DNP can influence the performance of OE-DNP, up to a factor of 5 when the mechanism is scalar-dominated. We identified features that should be considered for designing an optimal PA. Specifically, a localized spin density is preferred over a distributed one, because it increases the hyperfine coupling with the target nuclei. Secondly, the accessibility of the radical site, which affects the collision rate with the target molecule, should not be compromised by structural design (**BDPA**) or

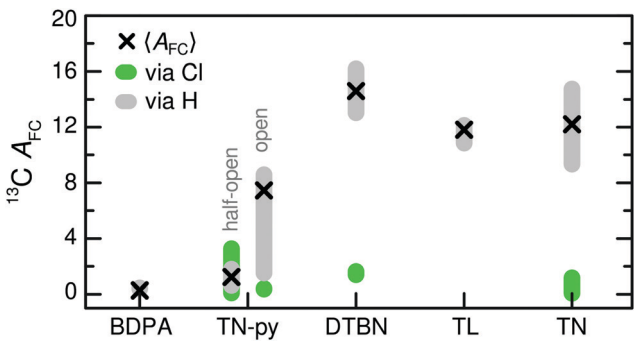

Fig. 4 Hyperfine coupling computed for geometry optimized complexes of PA/$CHCl_3$. The calculations were performed with Orca[47] using the basis set EPR-III for H, C, N, and O, and IGLO-II for Cl.[50] Two orientations of the $CHCl_3$ are considered ("*via* H" and "*via* Cl"). $\langle A_{FC}\rangle$ is the weighed average with respect to the relative energy of each configuration.

conformational rearrangements (**TN-py**). We note that these characteristics, which can be inferred *a priori* from the structure of the PA, affect the field independent term of the scalar relaxation and should therefore be taken into account also for OE-DNP at high magnetic fields.

Conflicts of interest

There are no conflicts to declare.

Acknowledgements

Financial support has been provided by the Max Planck Society. M. L. acknowledges IMPRS-PBCS of the Max Planck Society for funding for a fellowship. The Synthetic Chemistry facility of MPI-bpc is acknowledged for the synthesis of the radical **TN-py**. Open Access funding provided by the Max Planck Society.

Notes and references

1 J. H. Ardenkjaer-Larsen, G. S. Boebinger, A. Comment, S. Duckett, A. S. Edison, F. Engelke, C. Griesinger, R. G. Griffin, C. Hilty, H. Maeda, G. Parigi, T. Prisner, E. Ravera, J. v. Bentum, S. Vega, A. Webb, C. Luchinat, H. Schwalbe and L. Frydman, *Angew. Chem., Int. Ed.*, 2015, **54**, 9162–9185.
2 *Handbook of High Field Dynamic Nuclear Polarization*, ed. V. K. Michaelis, R. G. Griffin, B. Corzilius and S. Vega, Wiley, 2019.
3 A. S. L. Thankamony, J. J. Wittmann, M. Kaushik and B. Corzilius, *Prog. Nucl. Magn. Reson. Spectrosc.*, 2017, **102–103**, 120–195.
4 T. Kobayashi and M. Pruski, *ACS Catal.*, 2019, **9**, 7238–7249.
5 C. Song, K.-N. Hu, C.-G. Joo, T. M. Swager and R. G. Griffin, *J. Am. Chem. Soc.*, 2006, **128**, 11385–11390.
6 C. Sauvee, M. Rosay, G. Casano, F. Aussenac, R. T. Weber, O. Ouari and P. Tordo, *Angew. Chem., Int. Ed.*, 2013, **52**, 10858–10861.
7 G. Casano, H. Karoui and O. Ouari, *eMagRes*, 2018, 195–208.
8 K. H. Hausser and D. Stehlik, *Adv. Magn. Reson.*, 1968, **3**, 79–139.
9 M. Bennati and T. Orlando, *eMagRes*, 2019, 11–18.
10 V. P. Denysenkov and T. F. Prisner, *eMagRes*, 2019, 41–54.
11 V. Denysenkov, M. J. Prandolini, M. Gafurov, D. Sezer, B. Endeward and T. F. Prisner, *Phys. Chem. Chem. Phys.*, 2010, **12**, 5741–5751.
12 P. J. van Bentum, G. H. A. van der Heijden, J. A. Villanueva-Garibay and A. P. Kentgens, *Phys. Chem. Chem. Phys.*, 2011, **13**, 17831.
13 P. Neugebauer, J. G. Krummenacker, V. P. Denysenkov, C. Helmling, C. Luchinat, G. Parigi and T. F. Prisner, *Phys. Chem. Chem. Phys.*, 2014, **16**, 18781–18787.
14 T. Dubroca, A. N. Smith, K. J. Pike, S. Froud, R. Wylde, B. Trociewitz, J. McKay, F. Mentink-Vigier, J. van Tol, S. Wi, W. Brey, J. R. Long, L. Frydman and S. Hill, *J. Magn. Reson.*, 2018, **289**, 35–44.
15 D. Yoon, A. I. Dimitriadis, M. Soundararajan, C. Caspers, J. Genoud, S. Alberti, E. de rijk and J.-P. Ansermet, *Anal. Chem.*, 2018, **90**, 5620–5626.
16 M. D. Lingwood, T. A. Siaw, N. Sailasuta, B. D. Ross, P. Bhattacharya and S. Han, *J. Magn. Reson.*, 2010, **205**, 247–254.
17 V. P. Denysenkov, M. Terekhov, R. Maeder, S. Fischer, S. Zangos, T. Vogl and T. F. Prisner, *Sci. Rep.*, 2017, **7**, 44010.
18 S. Stevenson and H. C. Dorn, *Anal. Chem.*, 1994, **66**, 2993–2999.
19 S. van Meerten, F. van Zelst, K. Tijssen and A. Kentgens, *Anal. Chem.*, 2020, **92**, 13010–13016.
20 B. Gizatullin, C. Mattea and S. Stapf, *J. Magn. Reson.*, 2019, **307**, 106583.
21 B. D. Armstrong and S. Han, *J. Am. Chem. Soc.*, 2009, **131**, 4641–4647.
22 J. R. Biller, R. Barnes and S. Han, *Curr. Opin. Colloid Interface Sci.*, 2018, **33**, 72–85.
23 O. Jakdetchai, V. Denysenkov, J. Becker-Baldus, B. Dutagaci, T. F. Prisner and C. Glaubitz, *J. Am. Chem. Soc.*, 2014, **136**, 15533–15536.
24 T. Orlando, R. Dervisoglu, M. Levien, I. Tkach, T. F. Prisner, L. Andreas, V. Denysenkov and M. Bennati, *Angew. Chem., Int. Ed.*, 2019, **58**, 1402–1406.
25 T. J. Keller, A. J. Laut, J. Sirigiri and T. Maly, *J. Magn. Reson.*, 2020, **313**, 106719.
26 M. Lingwood and S. Han, *Annu. Rep. NMR Spectrosc.*, 2011, **73**, 83–126.
27 C. Griesinger, M. Bennati, H. M. Vieth, C. Luchinat, G. Parigi, P. H. Engelke, S. J. Glaser, V. Denysenkov and T. F. Prisner, *Prog. Nucl. Magn. Reson. Spectrosc.*, 2012, **64**, 4–28.
28 R. A. Wind and J. H. Ardenkjær-Larsen, *J. Magn. Reson.*, 1999, **141**, 347–354.
29 P. Hoefer, G. Parigi, C. Luchinat, P. Carl, G. Guthausen, M. Reese, T. Carlomagno, C. Griesinger and M. Bennati, *J. Am. Chem. Soc.*, 2008, **130**, 3254–3255.
30 M.-T. Tuerke, G. Parigi, C. Luchinat and M. Bennati, *Phys. Chem. Chem. Phys.*, 2012, **14**, 502–510.
31 M.-T. Tuerke and M. Bennati, *Phys. Chem. Chem. Phys.*, 2011, **13**, 3630–3633.
32 N. Enkin, G. Liu, M. del C. Gimenez-Lopez, K. Porfyrakis, I. Tkach and M. Bennati, *Phys. Chem. Chem. Phys.*, 2015, **17**, 11144–11149.
33 N. M. Loening, M. Rosay, V. Weis and R. G. Griffin, *J. Am. Chem. Soc.*, 2002, **124**, 8808–8809.
34 T. V. Can, M. A. Caporini, F. Mentink-Vigier, B. Corzilius, J. J. Walish, M. Rosay, W. E. Maas, M. Baldus, S. Vega, T. M. Swager and R. G. Griffin, *J. Chem. Phys.*, 2014, **141**, 064202.
35 M. Bennati, C. Luchinat, G. Parigi and M.-T. Tuerke, *Phys. Chem. Chem. Phys.*, 2010, **12**, 5902–5910.
36 G. H. A. van der Heijden, A. P. M. Kentgens and P. J. M. van Bentum, *Phys. Chem. Chem. Phys.*, 2014, **16**, 8493–8502.
37 M. D. Lingwood and S. Han, *J. Magn. Reson.*, 2009, **201**, 137–145.

Open Access Article. Published on 05 February 2021. Downloaded on 2/8/2026 9:11:54 PM. This article is licensed under a Creative Commons Attribution 3.0 Unported Licence.

Open Access Article. Published on 05 February 2021. Downloaded on 2/8/2026 9:11:54 PM.
This article is licensed under a Creative Commons Attribution 3.0 Unported Licence.

38 X. Wang, W. C. Isley, S. Salido, Z. Sun, L. Song, C. J. Cramer and H. Dorn, *Chem. Sci.*, 2015, **6**, 6482–6495.
39 M. Levien, M. Hiller, I. Tkach, M. Bennati and T. Orlando, *J. Phys. Chem. Lett.*, 2020, **11**, 1629–1635.
40 E. Ravera, C. Luchinat and G. Parigi, *J. Magn. Reson.*, 2016, **264**, 78–87.
41 W. Müller-Warmuth, R. Vilhjalmsson, P. Gerlof, J. Smidt and J. Trommel, *Mol. Phys.*, 1976, **31**, 1055–1067.
42 G. Liu, M. Levien, N. Karschin, G. Parigi, C. Luchinat and M. Bennati, *Nat. Chem.*, 2017, **9**, 676–680.
43 L.-P. Hwang and J. H. Freed, *J. Chem. Phys.*, 1975, **63**, 4017–4025.
44 C. F. Polnaszek and R. G. Bryant, *J. Chem. Phys.*, 1984, **81**, 4038–4045.
45 A. N. Tikhonov, L. N. Ikryannikova and L. Y. Ustynyuk, *Magn. Reson. Chem.*, 2010, **48**, 337–349.
46 H. H. Haeri, P. Spindler, J. Plackmeyer and T. Prisner, *Phys. Chem. Chem. Phys.*, 2016, **18**, 29164–29169.
47 F. Neese, *Wiley Interdiscip. Rev.: Comput. Mol. Sci.*, 2012, **2**, 73–78.
48 E. F. Pettersen, T. D. Goddard, C. C. Huang, G. S. Couch, D. M. Greenblatt, E. C. Meng and T. E. Ferrin, *J. Comput. Chem.*, 2004, **25**, 1605–1612.
49 G. Stevanato, G. Casano, D. J. Kubicki, Y. Rao, L. Esteban Hofer, G. Menzildjian, H. Karoui, D. Siri, M. Cordova, M. Yulikov, G. Jeschke, M. Lelli, A. Lesage, O. Ouari and L. Emsley, *J. Am. Chem. Soc.*, 2020, **142**, 16587–16599.
50 W. Kutzelnigg, U. Fleischer and C. van Wüllen, Shielding Calculations: IGLO Method, in *eMagRes*, ed. R. K. Harris and R. L. Wasylishen, 2007, DOI: 10.1002/9780470034590.emrstm0495.
51 K. Sakai, K.-i. Yamada, T. Yamasaki, Y. Kinoshita, F. Mito and H. Utsumi, Effective 2,6-substitution of piperidine nitroxyl radical by carbonyl compound, *Tetrahedron*, 2010, **66**(13), 2311–2315, DOI: 10.1016/j.tet.2010.02.004.
52 Jmol: an open-source Java viewer for chemical structures in 3D, http://www.jmol.org/.